https://doi.org/10.5194/gmd-2020-102
Preprint. Discussion started: 24 June 2020
© Author(s) 2020. CC BY 4.0 License.

Geoscientific Model Development Discussions
Open Access

Evaluation of polar stratospheric clouds in the global chemistry-climate model SOCOLv3.1 by comparison with CALIPSO spaceborne lidar measurements

Michael Steiner[1,*], Beiping Luo[1], Thomas Peter[1], Michael C. Pitts[2], and Andrea Stenke[1]

[1]Institute for Atmospheric and Climate Science, ETH Zurich, Switzerland
[*]now at Laboratory for Air Pollution / Environmental Technology, EMPA, Switzerland
[2]NASA Langley Research Center, Hampton, Virginia 23681, USA

Correspondence: Michael Steiner (michael.steiner@empa.ch)

Abstract. Polar Stratospheric Clouds (PSCs) contribute to catalytic ozone destruction by providing surfaces for the conversion of inert chlorine species into active forms and by denitrification of the stratosphere. Therefore, an accurate representation of PSCs in chemistry-climate models (CCMs) is of great importance to correctly simulate polar ozone concentrations. Here, we evaluate PSCs as simulated by the CCM SOCOLv3.1 for the Antarctic winter 2007 by comparison with backscatter measurements by CALIOP onboard the CALIPSO satellite. The model considers supercooled ternary solution (STS) droplets, nitric acid trihydrate (NAT) particles, water ice particles, and mixtures thereof. PSCs are parametrized in terms of temperature and partial pressures of HNO_3 and H_2O, assuming equilibrium between gas and particulate phase. We use the CALIOP measurements to optimize three prescribed microphysical parameters of the PSC scheme, namely ice number density, NAT particle radius and maximum NAT number density. The choice of the prescribed value of the ice number density affects simulated optical properties and dehydration, while modifying the maximum NAT number density or the NAT particle radius impacts stratospheric composition by enhancing the HNO_3-uptake and denitrification. Best agreement with the CALIOP optical properties and observed denitrification was for this case study found with the ice number density increased from the hitherto used value of 0.01 to 0.05 cm^{-3} and the maximum NAT number density from 5×10^{-4} to 1×10^{-3} cm^{-3}. The NAT radius was kept at the original value of 5 µm. The new parametrization reflects the higher importance attributed to heterogeneous nucleation of ice and NAT particles, e.g. on meteoric dust, following recent new data evaluations of the state-of-the-art CALIOP measurements. A cold temperature bias in the polar lower stratosphere results in an overestimated PSC areal coverage in SOCOLv3.1 by up to 100%. Furthermore, the occurrence of mountain-wave induced ice, as observed mainly over the Antarctic Peninsula, is continuously underestimated in the model due to the coarse model resolution and the fixed ice number density. However, overall we find a good temporal and spatial agreement between modeled and observed PSC occurrence and composition, as well as reasonable modeled denitrification and ozone loss. Based on constraining three important parameters by means of the CALIOP measurements, this work demonstrates that also a simplified PSC scheme, which describes STS, NAT, ice and mixtures thereof with equilibrium assumptions and avoids nucleation and growth calculations in sophisticated, but time-consuming microphysical process models, may achieve good approximations of fundamental properties of PSCs needed in CCMs.

https://doi.org/10.5194/gmd-2020-102
Preprint. Discussion started: 24 June 2020
© Author(s) 2020. CC BY 4.0 License.

Geoscientific Model Development Discussions
Open Access

1 Introduction

Although the occurrence of clouds in the wintertime polar stratosphere has been observed for a long time, their importance for stratospheric ozone depletion was only recognized after the discovery of the Antarctic ozone hole in the mid 1980s (Farman et al., 1985). Stratospheric clouds composed of supercooled ternary solutions (STS, H_2SO_4-HNO_3-H_2O mixtures), crystalline nitric acid trihydrate (NAT) and water ice provide surfaces, on which inert reservoir species like HCl and $ClONO_2$ are transformed into active forms (Solomon et al., 1986). The activated species then are responsible for springtime ozone depletion induced by catalytic cycles (Molina and Molina, 1987). While STS droplets are responsible for most of the chlorine activation (Portmann et al., 1996; Kirner et al., 2015, and references therein), solid particles can in addition strongly affect the chemical composition of the stratosphere. Especially NAT particles can, under certain conditions, grow to large particles with diameters of up to 20 μm, so-called NAT-rocks (Fahey et al., 2001). Their number density is small (Biele et al., 2001), but due to their size they reach high settling velocities and by sedimentation remove reactive nitrogen from the stratosphere. This so-called denitrification contributes to ozone depletion by hindering the formation of inactive reservoir species (Salawitch et al., 1993).

While the formation of water ice requires extremely cold conditions in the dry stratosphere, HNO_3-containing particles already occur at higher temperatures (Hanson and Mauersberger, 1988), and hence much more frequently. In contrast to solid particles, there is no nucleation barrier for liquid STS droplets, which form upon uptake of HNO_3 and H_2O from the gas-phase by binary H_2SO_4-H_2O solution droplets (Carslaw et al., 1995). Depending on the presence or absence of heterogeneous nuclei, different pathways of PSC formation exist (e.g. Fig. 2 in Hoyle et al., 2013).

PSCs are observed by ground-based lidar instruments (e.g. Biele et al., 2001; Simpson et al., 2005), in airborne campaigns (e.g. Fahey et al., 2001) or by space-borne satellites (e.g. Michelson Interferometer for Passive Atmospheric Soundings; Fischer and Oelhaf, 1996; Fischer et al., 2008). Since 2006 the Cloud-Aerosol Lidar with Orthogonal Polarization (CALIOP) on CALIPSO (Cloud-Aerosol Lidar and Infrared Pathfinder Satellite Observations) measures PSCs with high vertical resolution (Winker and Pelon, 2003; Winker et al., 2007, 2009; Pitts et al., 2018). CALIOP measures backscatter intensities at 532 nm and 1064 nm wavelength, and additionally separates the 532 nm backscatter signal into parallel and perpendicular polarized components. The depolarization ratio is a measure of the particle shape and allows to distinguish between liquid (spherical) and solid (aspherical) particles. This makes CALIOP a very suitable tool for observing and classifying PSCs.

Due to their critical role in stratospheric chemistry, the representation of PSCs is indispensable for atmospheric chemistry models. However, the complexity of PSC schemes varies considerably between models. Some models primarily aim at mimicking the effects of PSCs on chemical composition and vertical re-distribution of HNO_3 and H_2O rather than at exactly reproducing PSC compositions. The detailed PSC formation along different pathways, depending on the presence or absence of heterogeneous nuclei, is usually not taken into account in those models. This is no problem under many circumstances, e.g. when chlorine activation is close to saturation in the middle of an Antarctic winter, but an accurate knowledge of the heterogeneous reaction and denitrification rates is essential for a quantitative description of polar ozone chemistry under transitional conditions, as they occur at winter onset or in late winter and early spring, or at the far edge of the vortex. Therefore, some

https://doi.org/10.5194/gmd-2020-102
Preprint. Discussion started: 24 June 2020
© Author(s) 2020. CC BY 4.0 License.
Geoscientific Model Development Discussions

models include PSCs in a more sophisticated manner and aim at correctly simulating nucleation, growth and sedimentation of the different PSC types as well as the detailed redistribution of HNO_3 and H_2O.

Simple parametrizations form NAT or ice instantaneously either at the saturation temperature, or at a certain supersaturation. Below the onset temperature of NAT or ice, excess matter of HNO_3 or H_2O is directly transferred into the particulate phase, assuming equilibrium. The particle size then depends on assumptions made about the number density distribution or vice versa. Examples for global chemistry models using such PSC parametrizations are SOCOLv3.1 (Stenke et al., 2013), LMDZrepro (Jourdain et al., 2008) or CCSRNIES (Akiyoshi et al., 2009). More complex PSC schemes allow deviations from thermodynamic equilibrium and explicitly simulate nucleation, growth and evaporation of particles, as in CLaMS (Tritscher et al., 2019) or WACCM/CARMA (Garcia et al., 2007; Bardeen et al., 2013; Zhu et al., 2017). As particle sedimentation is important for the chemical composition of the stratosphere, it is included in all PSC schemes. The settling velocity is mainly dependent on particle size, which is either described by a modal size distribution (e.g. SOCOL, LMDZrepro), size bins (e.g. SWACCM/CARMA, EMAC (Khosrawi et al., 2018), BIRA (Daerden et al., 2007)) or as single representative particles in models with Lagrangian sedimentation schemes (e.g. SCLaMS, ATLAS (Wohltmann et al., 2010), SLIMCAT/TOMCAT (Feng et al., 2011)). A detailed overview over the representation of PSCs in global models and its evaluation can be found in Grooß et al. (2020, in prep.).

Different approaches have been used to investigate the performance of PSC schemes, ranging from the evaluation of bulk properties like PSC areal coverage or air volume covered by PSCs up to detailed assessments of PSC properties along single satellite orbits. In addition, the impacts of PSCs on the chemical composition or chlorine activation can be evaluated by comparison with observations of certain chemical species. Tritscher et al. (2019) recently presented a detailed evaluation of PSCs in CLaMS, including optical properties, geographical PSC volume, along-orbit comparisons and influence on gas-phase HNO_3 and H_2O. Simulations for the Arctic winter 2009/2010 and the Antarctic winter 2011 show good agreement with observations. However, the simulated HNO_3-uptake in early winter was stronger than observed and the permanent redistribution of HNO_3 was underestimated. A new PSC model in WACCM/CARMA, taking into account detailed microphysical processes, was presented by Zhu et al. (2017). They extensively compared the PSCs in the Antarctic winter 2010 with CALIOP-observations and examined modeled gas-phase HNO_3 and H_2O distributions. They found the derived optical properties of PSCs and the denitrification to be well reproduced by the model. However, PSCs with small NAT particles and large number densities were underestimated, which might be caused by a missing NAT formation pathway on ice particles (Zhu et al., 2017). Other studies focused mainly on the impact of PSCs by comparing HNO_3 and H_2O with space-borne observations from MLS (Microwave Limb Sounder; Waters et al., 2006; Schoeberl, 2007), MIPAS or with airborne measurements. The study by Khosrawi et al. (2018), evaluating EMAC for the Arctic winters 2009/2010 and 2010/2011, found good agreement for the temporal evolution of gas-phase HNO_3 in the polar stratosphere, but simulated PSC volumes were smaller than observed by MIPAS. Recently, Snels et al. (2019) presented a statistical comparison including several models from CCMVal-2 and CCMI project with observations. They used a set of diagnostics, based on spatial distribution of ice and NAT surface area densities and temperature, to compare simulated PSCs among the different CCMs. They concluded that the geographical distribution of PSCs in the polar vortex, as observed by CALIOP, is not well reproduced by the models. The models showed a limited ability to reproduce the longitudinal variations in PSC occurrences and mostly overestimate NAT and ice occurrence, most probably due to a cold

https://doi.org/10.5194/gmd-2020-102
Preprint. Discussion started: 24 June 2020
© Author(s) 2020. CC BY 4.0 License.
Geoscientific Model Development Discussions

temperature bias. WACCM-CCMI (Garcia et al., 2017), where the cold bias was reduced by introducing additional mechanical forcing of the circulation via parametrized gravity waves, compared best with observations.

In this study, we compare a simple equilibrium scheme of STS, NAT, ice and mixtures thereof with state-of-the-art PSC satellite data, aiming to optimize the scheme for economic and efficient use in a chemistry-climate model (CCM). To this end, we evaluate the representation of PSCs in the CCM SOCOLv3.1 for the Antarctic winter 2007. We convert the simulated PSCs into an optical signal to mimick a satellite measurement and compare the results with CALIPSO observations. We further evaluate the impacts of the simulated PSCs on the chemical composition of the stratosphere by comparison with satellite observations of HNO_3, H_2O and O_3. A more detailed description of our methodology and the datasets utilized is given in Sect. 2. In Sect. 3 we present the results of the comparison, and Sect. 4 provides conclusions.

2 Model description and observational data

2.1 The SOCOLv3.1 chemistry-climate model

The state-of-the-art chemistry-climate model SOCOLv3.1 (Stenke et al., 2013; Revell et al., 2015) is based on the middle-atmosphere general circulation model (GCM) MA-ECHAM5 (European Centre/HAMburg climate model; Roeckner et al., 2006), coupled to the chemistry module MEZON (Model for Evaluation of oZONe trends; Egorova et al., 2003). MEZON contains 57 chemical species, 56 photolysis reactions, 184 gas-phase reactions and 16 heterogeneous reactions in and on aqueous sulfuric acid aerosols as well as three types of PSCs, namely STS droplets, NAT and water ice. Heterogeneous hydrolysis of N_2O_5 on tropospheric aerosols is as well taken into account. The chemistry module MEZON covers stratospheric ozone chemistry in detail as well as the tropospheric background chemistry, including the oxidation of isoprene (Pöschl et al., 2000). The coupling between the GCM and the chemistry module takes place through simulated winds and temperatures, as well as through the radiative forcing caused by ozone, methane, nitrous oxide, water vapor and CFCs. The dynamical time step is 15 min, whereas the radiation and chemistry schemes are called every 2 h.

The parametrization of PSCs in MEZON includes the three PSC types water ice, NAT and STS. STS droplets form upon the uptake of gas-phase HNO_3 and H_2O by aqueous sulfuric acid aerosols (supercooled binary solutions, SBS), following the expression by Carslaw et al. (1995). In SOCOLv3.1, the binary aerosols are prescribed as a time series of observed monthly mean sulfate aerosol surface area density, mainly based on SAGE (Stratospheric Aerosol and Gas Experiment) observations (Stenke et al., 2013). NAT is formed if the HNO_3 partial pressure exceeds its saturation pressure (Hanson and Mauersberger, 1988). For NAT particles, a mean radius of 5 µm is assumed, and the maximum number density is set to $5{\cdot}10^{-4}$ cm^{-3}. This limitation accounts for the observational evidence that NAT clouds are often strongly supersaturated and prevents condensation of all available gas-phase HNO_3 onto NAT particles. The assumptions of $n_{NAT,max}$=$5{\cdot}10^{-4}$ cm^{-3} and r_{NAT}=5 µm allow for $\sim$10% of the HNO_3 at beginning of winter to be taken up into NAT particles (0.77 ppbv at 50 hPa and 195 K, assuming 5 ppmv H_2O). For water ice, a particle number density of 0.01 cm^{-3} is prescribed. This represents the background ice number density but not ice formed in mountain waves, where very high nucleation rates result in much higher ice number densities of $\sim$ 5-10 cm^{-3} (Hu et al., 2002) and particle sizes of $<$3 µm (Höpfner et al., 2006). For water ice particles as well as for

https://doi.org/10.5194/gmd-2020-102
Preprint. Discussion started: 24 June 2020
© Author(s) 2020. CC BY 4.0 License.

STS droplets the PSC routine assumes thermodynamic equilibrium with the gas-phase. Sedimentation of solid PSC particles is included. The fall velocities of NAT and ice particles are based on Stokes theory (described in Pruppacher and Klett, 1997). Advection of PSC particles is not explicitly calculated in SOCOL, but at the end of each chemical time step all condensed HNO_3 and H_2O evaporates back to the gas phase. To prevent spurious PSC formation caused by potential model temperature, HNO_3 and/or H_2O biases in regions where PSCs are usually not observed, and to avoid overlap with the regular cloud scheme of the GCM, the occurrence of PSCs is spatially restricted. Water ice particles are allowed to occur between 130 hPa and 11 hPa and polewards of 50°N/S. NAT particles are allowed between the tropopause and 11 hPa. STS and NAT particles may form at all latitudes.

For the present study SOCOLv3.1 was run with T42 horizontal resolution (about 2.8°x 2.8°in latitude and longitude) and 39 vertical levels between the surface and the model top centered at 0.01 hPa (∼80 km). In order to allow for a direct comparison with observations, the model was run in specified dynamics mode, i.e. the prognostic variables temperature, vorticity, divergence and the logarithm of the surface pressure are relaxed towards ERA-Interim reanalysis data (Dee et al., 2011). We applied a uniform nudging strength throughout the whole model domain, with a relaxation timescale of 24 h for temperature and logarithm of the surface pressure, 48 h for divergence and 6 h for vorticity. The boundary conditions follow the specifications of the reference simulation REF-C1 of phase 1 of the Chemistry Climate Model Initiative (CCMI-1; Morgenstern et al., 2017). All simulations for this study were run between 01 May 2007 and 31 October 2007 with a 12-hourly output time step. We chose 2007 for our evaluation, which represents an average winter in terms of PSC occurrence, while data coverage for CALIPSO was rather high.

2.2 CALIPSO PSC observations

The simulated PSCs in SOCOL are compared to measurements from the CALIOP instrument onboard CALIPSO, an Earth observation satellite in the A-train constellation in operation since 2006 (Winker and Pelon, 2003; Winker et al., 2007, 2009). The A-train of satellites orbits the Earth 14-15 times per day, covering the latitudes between 82°S and 82°N on each orbit. CALIOP is a dual-wavelength lidar with three receiver channels, one measuring the 1064 nm backscatter intensity, the two others measuring the parallel and perpendicular polarized components ($\beta_{\parallel}$ and $\beta_{\perp}$) of the 532 nm backscattered signal. The frequency of the lidar pulse is 20.25 Hz, corresponding to one measurement every 333 m along the flight track. From the measured backscatter coefficients (e.g. β_{532}) the total (sum of particulate and molecular) to molecular backscatter ratio

$$R_{532} = \frac{\beta_{532}}{\beta_{\mathrm{m}}} = \frac{\beta_{\mathrm{part,532}} + \beta_{\mathrm{m}}}{\beta_{\mathrm{m}}} \tag{1}$$

can be calculated, with β_{m} being the molecular backscatter coefficient. β_{m} is calculated as described in Hostetler et al. (2006) using molecular number density profiles provided by the MERRA-2 (Modern-Era Retrospective analysis for Research and Applications, version 2) reanalysis products (Gelaro et al., 2017). With the separation of the 532 nm backscatter signal into parallel and perpendicular polarized components, the depolarization ratio ($\delta_{\mathrm{aerosol}}$, i.e. the perpendicular to parallel component) of the 532 nm signal can be derived, which is an indicator of the particle shape and hence phase (liquid/solid).

https://doi.org/10.5194/gmd-2020-102
Preprint. Discussion started: 24 June 2020
© Author(s) 2020. CC BY 4.0 License.
Geoscientific Model Development Discussions

In this study we use the Lidar Level 2 Polar Stratospheric Cloud Mask Product (available via Michael C. Pitts), which was derived with version 2 (v2) of the PSC detection algorithm (Pitts et al., 2018) from the CALIOP v4.10 Lidar Level 1B data products. This CALIOP PSC dataset contains profiles of PSCs with classification and optical properties, also providing temperature, pressure and tropopause height derived from MERRA-2 reanalyses. The spatial resolution of PSC data is 5 km in the horizontal by 180 m in the vertical. Only night-time measurements are considered. For this study, CALIPSO data from 01 May 2007 to 31 October 2007 are used.

Version 2 of the detection algorithm (Pitts et al., 2018) detects PSCs as statistical outliers in either $\beta_{\perp}$ or R_{532}, relative to the background stratospheric aerosols population. The optical properties of stratospheric background aerosol are derived from CALIOP measurements above 200 K. Both thresholds are defined as median plus one median absolute deviation. They are calculated daily and vary with potential temperature. Furthermore, additional averaging (over 15, 45 and 135 km) has been implemented into the PSC detection algorithm to enable the detection of more tenuous clouds than at 5 km resolution only.

The PSC classification in Pitts et al. (2018) distinguishes STS, STS-NAT mixtures, enhanced NAT mixtures, ice and wave ice. The categories are visualized in Fig. 1. The dotted lines denote dynamical boundaries, while the solid lines show boundaries at fixed $\beta_{\perp}$ or R_{532} values. The lines at the lower left corner approximate the $\beta_{\perp}$-threshold ($\beta_{\perp,\mathrm{thresh}}$) and R_{532}-threshold ($R_{532,\mathrm{thresh}}$), respectively. All PSCs above $\beta_{\perp,\mathrm{thresh}}$ are assumed to contain non-spherical particles. The boundary between the two NAT mixture categories and ice is calculated "dynamically", i.e. based on cloud-free MLS measurements of $\mathrm{HNO_3}$ and $\mathrm{H_2O}$. PSCs are detected as wave ice when they contain non-spherical particles and if R_{532}>50. A detailed description of the classification scheme is given in Pitts et al. (2018). PSC observations of July 2007 (Fig. 1) show the most distinct relative maxima for STS. Two further relative maxima appear with higher $\delta_{\mathrm{aerosol}}$ values, indicating solid particles. The relative maximum extending towards the upper left corner of the histogram corresponds to STS-NAT mixtures with low NAT number densities (n_{NAT}), while the second relative maximum extending towards the upper right corresponds to mixtures of NAT with high number densities and ice as well as to wave ice PSCs.

2.3 MLS observations

In this study, modeled $\mathrm{HNO_3}$, $\mathrm{H_2O}$ and $\mathrm{O_3}$ mixing ratios are compared to satellite measurements of the instrument Microwave Limb Sounder (MLS) onboard the Aura satellite (Waters et al., 2006). MLS measures atmospheric profiles by scanning from the ground to 90 km height in flight direction, passively measuring microwave thermal emissions. All three quantities are derived by version 4.2 from the Aura MLS Level 2 data (Livesey et al., 2018). The $\mathrm{HNO_3}$ dataset has a vertical resolution of approximately 3-4 km vertical resolution, while the $\mathrm{H_2O}$ and $\mathrm{O_3}$ datasets have a vertical resolution of 2.5 to 3 km. The accuracy of the MLS measurements is 1-2 ppbv for $\mathrm{HNO_3}$ (Santee et al., 2007), 4%-7% for $\mathrm{H_2O}$ (Read et al., 2007; Lambert et al., 2007) and 8% for stratospheric $\mathrm{O_3}$ (Jiang et al., 2007). Detailed informations and a precise description of the dataset can be found in Livesey et al. (2018).

https://doi.org/10.5194/gmd-2020-102
Preprint. Discussion started: 24 June 2020
© Author(s) 2020. CC BY 4.0 License.

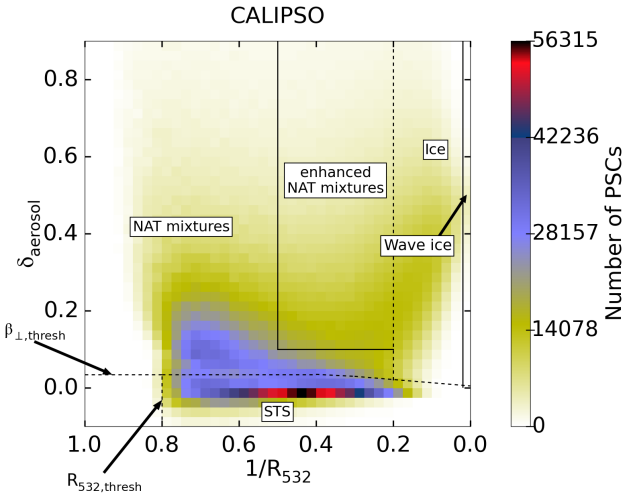

Figure 1. Composite 2D-histogram of CALIPSO PSC measurements of July 2007 in a $1/R_{532}$-δ_{aerosol} coordinate system with 40x40 bins. The colors indicate the number of PSC measurements in one bin. Dotted lines denote dynamical classification boundaries or thresholds and solid lines denote fixed classification boundaries.

2.4 Model-measurement comparison

While CALIOP measures backscatter signals and depolarization ratios, the SOCOL model provides surface area densities (SAD) for STS, NAT and water ice as function of pressure, latitude and longitude. From the simulated SADs and the assumed microphysical parameters, we calculate the number density and/or radius for each particle type. This information is used in Mie and T-matrix scattering codes (Mishchenko et al., 1996) to compute optical parameters of the simulated PSCs, i.e. R_{532}, δ_{aerosol} and $\beta_{\perp}$, for comparison with CALIOP observations. For NAT and ice particles, circular symmetric spheroids with an aspect ratio of 0.9 are assumed. Refractive indices of 1.31 for ice and 1.48 for NAT were chosen. The CALIOP PSC data product includes both detection threshold values, $R_{532,\text{thresh}}$ and $\beta_{\perp,\text{thresh}}$, for each measurement. To achieve a better comparability between model and observations, these daily threshold values are also applied on the calculated optical properties of the PSCs simulated by SOCOL. For this purpose, we calculated the daily mean thresholds from all observations for each pressure level. This procedure is essential for a fair comparison between model and satellite data, as the geographical PSC extent strongly depends on these detection limits.

To ensure best possible comparability between model and measurements, observational uncertainties have to be applied to the calculated optical properties of the modeled PSCs. We followed the approach by Engel et al. (2013). The uncertainty scales inversely to the square root of the horizontal averaging distance along a flight path, which we set to 135 km. This value corresponds to the best case for detection, which maximizes the comparability with the model (which obviously does not have a detection threshold). An example for the added measurement noise is shown in Fig. 2. When looking at the individual PSC types (Fig. 2a), STS and NAT, due to their spherical shape and fixed radius, appear at constant δ_{aerosol}-values of 0 and 0.167,

https://doi.org/10.5194/gmd-2020-102
Preprint. Discussion started: 24 June 2020
© Author(s) 2020. CC BY 4.0 License.

Geoscientific Model Development
Discussions

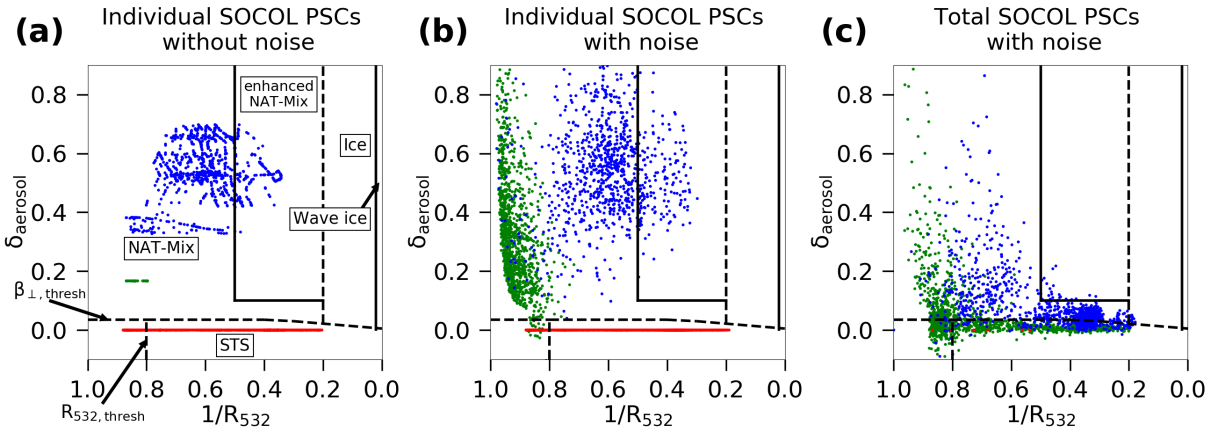

Figure 2. Scatter plot of simulated PSCs in SOCOL on 01 July 2007 in a $1/R_{532}$-δ_{aerosol} coordinate system. (a): STS (red), NAT (green) and ice (blue) as individual components. (b): As in (a), but after applying observational uncertainties. (c): The modeled PSCs as mixture of all components present per grid box (red: pure STS, green: STS-NAT mixtures, blue: mixtures with ice) with uncertainty.

respectively. The variable radius of ice particles results in a variable δ_{aerosol}-value. Applying the uncertainties to the parallel and the perpendicular backscatter coefficients primarily causes a large spread in depolarization ratio (Fig. 2b). When considering all PSC particles to be mixed within a grid box (Fig. 2c), their points are located mainly at the lower and left side of the composite histogram.

3 Results and discussion

3.1 Comparison along an orbit

As a first example we compare SOCOL with CALIPSO along a single flight track. Figure 3 shows a curtain of observed backscatter ratios R_{532} along orbit 2 on 01 July 2007 (Fig. 3a) and the corresponding PSC compositions (Fig. 3g). The observations show a large PSC over the Antarctic Peninsula (300°E - 270°E), and a smaller PSC over Oates Land (190°E - 160°E). Further, some tropospheric cirrus clouds were classified as PSCs. Above the Antarctic Peninsula, two distinctive regions with R_{532} values above 50 are evident. These high backscatter ratios are related to high number densities of ice particles (up to 10 cm^{-3}, Hu et al., 2002), which are caused by rapid cooling rates associated with mountain wave events. These wave ice clouds are surrounded by more synoptic scale PSCs with lower R_{532} values, which are classified as ice, STS and NAT mixtures.

Figures 3b and 3d show the corresponding plots for the PSCs as simulated by the SOCOL model in the respective grid boxes overflown by CALIPSO. Figures 3c and 3f show the same, but before detection thresholds and instrument uncertainty had been added. The model output also reveals a large PSC over the Antarctic Peninsula. However, the spatial extent of the simulated PSC is larger. The simulated backscatter ratio R_{532} peaks around 6, which is substantially lower than observed.

https://doi.org/10.5194/gmd-2020-102
Preprint. Discussion started: 24 June 2020
© Author(s) 2020. CC BY 4.0 License.
Geoscientific Model Development Discussions

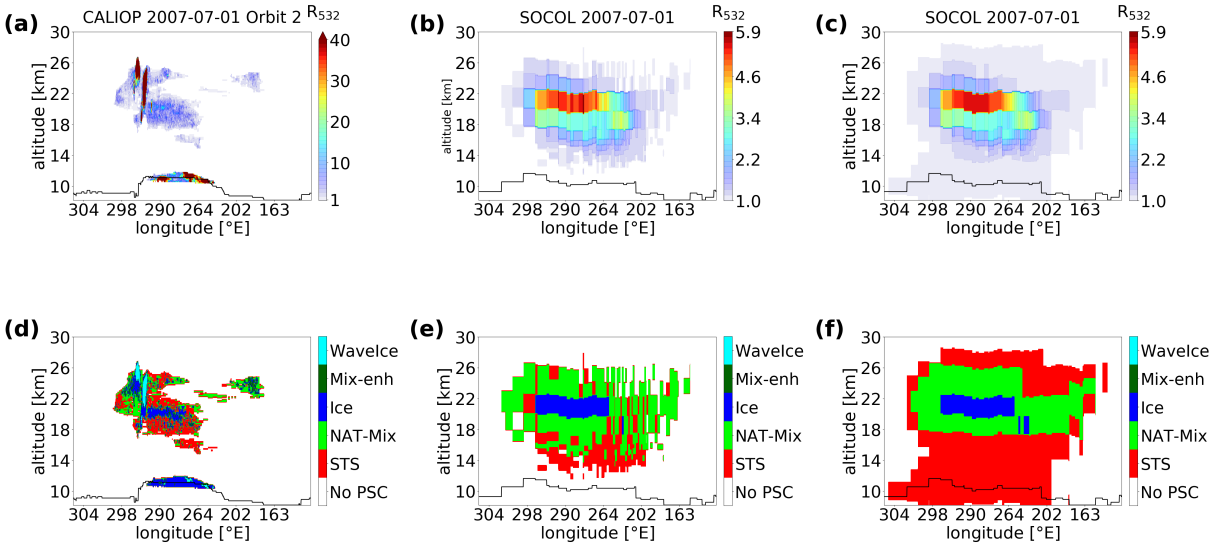

Figure 3. CALIPSO measurements on 01 July 2007 (orbit 2) of R_{532} (a) and the PSC classification (d). The calculated R_{532} values of modeled PSCs in the overflown grid boxes after adding the instrument uncertainty and applying the detection thresholds are shown in (b). (e) shows the composition of the corresponding PSCs according to the classification scheme in Pitts et al. (2018). (c and f): The same as in (b and e), but without instrument uncertainty and the detection thresholds. The black lines indicate the WMO and model tropopause height for CALIPSO measurements and simulations, respectively. Note the different color scales for CALIPSO (a) and model backscatter (b and c).

Due to the coarse resolution and orography, SOCOL is not able to capture high ice particle number densities associated with mountain wave events. Applying the CALIPSO classification scheme on the model output results in a layer of ice PSCs located around $\sim$20 km, which is slightly higher than in the observations. The ice cloud is surrounded by NAT mixtures, while the observations indicate STS. Below those NAT mixtures, pure STS clouds occur in the model, most of which are tenuous enough such that they fully disappear after applying the optical thresholds (Fig. 3e).

The actual modeled composition (see Appendix, Fig. A1) shows a similar pattern than the CALIPSO classification scheme, but with more ice Mix and less STS. These differences can also be seen in Fig. 2c, where most of the ice mixtures (blue) are located in the NAT-Mix domain, while many NAT mixtures (green) are located in the STS domain. It should be noted that the modeled optical properties are exclusively calculated for PSCs. Tropospheric cirrus clouds treated by the model's cloud routine are therefore excluded.

3.2 Spatial distribution

Figure 4 presents monthly mean (including clear-sky and cloudy-sky conditions) backscatter ratios R_{532} from observations and simulation for July (a and b) and August 2007 (c and d). For a better comparison the high-resolution measurements have been gridded onto the SOCOL grid. The data are vertically averaged over all pressure levels above the tropopause. The observations show a month-to-month variability in the location of the PSC region. In July 2007 the mean backscatter intensity appears more

https://doi.org/10.5194/gmd-2020-102
Preprint. Discussion started: 24 June 2020
© Author(s) 2020. CC BY 4.0 License.
Geoscientific Model Development Discussions
Open Access

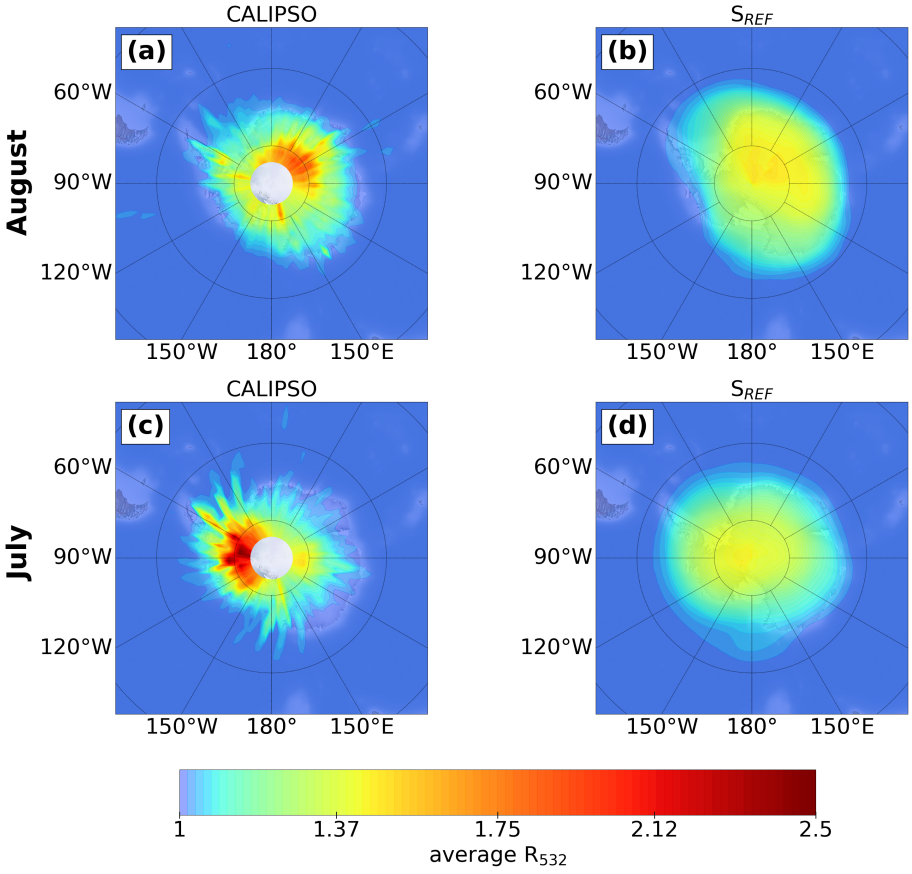

Figure 4. Gridded (on SOCOL grid) and vertically integrated monthly means of R_{532} for all-sky conditions as observed by CALIPSO (a and c) and simulated by SOCOL (b and d) for July (a and b) and August (c and d).

homogeneously distributed, with a slight peak over East Antarctica (∼0-150°E), while in August a distinct peak downstream of the Antarctic Peninsula (∼55-70°W) is observed. This characteristic feature is caused by the frequent mountain waves in this region (Hoffmann et al., 2017).

The modeled month-to-month variability of R_{532} values and areal extent agrees well with CALIPSO observations. In July, the center of the PSC area is also tilted towards East Antarctica and slightly towards the Peninsula in August. However, peak values of R_{532} are clearly lower for SOCOL. In comparison to the observations, the spatial distribution of SOCOL PSCs is more homogeneous. As mentioned above, this results mainly from a poor representation of mountain waves in the model.

3.3 PSC areal coverage

The total areal coverage as a function of altitude and time is a measure for the seasonal evolution of PSCs inside the polar vortex. Figure 5 compares CALIOP observations and model results for the winter 2007 (see also Fig. 13 in Pitts et al., 2018).

https://doi.org/10.5194/gmd-2020-102
Preprint. Discussion started: 24 June 2020
© Author(s) 2020. CC BY 4.0 License.

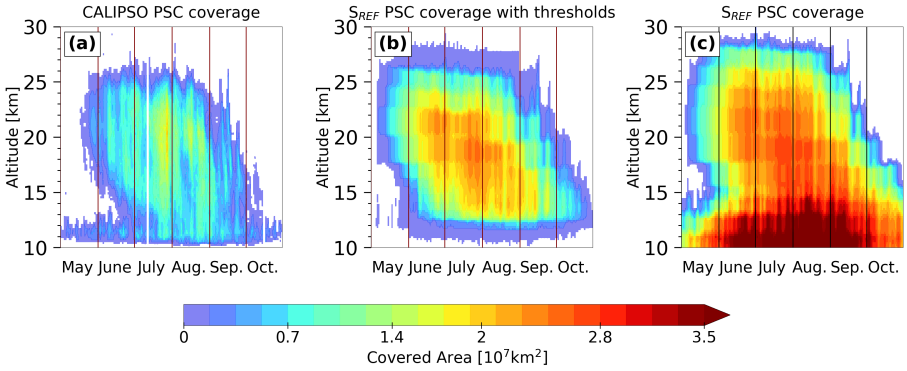

Figure 5. Time series of total PSC areal coverage over the Antarctic region as a function of altitude for the winter 2007 derived from CALIOP (a) and simulated by SOCOL as it would have been detected by the CALIOP (b). (c): the simulated PSC areal coverage without applied optical thresholds and without added uncertainty.

The observed PSC area is calculated from the daily fraction of PSC measurements within ten equal-sized latitude bands, while the modeled PSC area is determined for every grid box based on the PSC occurrence (above the detection thresholds) for two time steps per day. Since CALIOP does not measure poleward of 82°, measurements between 77.4 and 82°S are assumed to be representative of the entire 77.4–90°S latitude band.

Considering the low-level (11 - 12 km) clouds in May and June as tropospheric cirrus, the first PSC occurrence is observed in mid-May at 20-25 km altitude. Periods with higher PSC areal coverage with large vertical extent alternate with periods of less PSC extent. A clear peak occurs at end of July between 17 and 23 km altitude. The PSC areal coverage starts to decrease beginning of September, reaching zero mid-October. The descent of the coldest temperatures within the winter season is reflected in the descent of PSC occurrence. As described in Pitts et al. (2018), the PSCs merge with tropospheric cirrus clouds at mid-July.

In SOCOL PSC formation starts about 2 weeks earlier. The model is capable of reproducing the temporal occurrence of the individual peaks end of July. Also the overall descent of maximum PSC coverage is present in the simulation. PSC exist until end of October, which is longer than observed. However, SOCOL simulates a substantially larger PSC area, in particular between 13 and 23 km altitude, where $1.5{\cdot}10^7$ km^2 are almost continuously exceeded.

It is most likely that the different methods for calculating PSC areal coverage contributes to this overestimation. For each output time step, we considered the entire grid box to be covered by PSCs as soon as PSCs (above the detection thresholds) occur in the model. Further, also a cold-temperature bias in the model contributes to the larger PSC area.

The modeled PSC area calculated without the optical thresholds applied (Fig. 5c) is significantly larger, especially below 13 km altitude, where large areas with STS clouds occur in the model (see also Fig. 3f). Those large-scale STS clouds are very tenuous since they are filtered out by the conservative PSC detection threshold and hence do not play an important role in ozone chemistry. However, it highlights the crucial role of the detection thresholds when comparing PSC areas. Due to this sensitivity to the applied methods, quantitative comparisons of the areal coverage must be interpreted with caution.

https://doi.org/10.5194/gmd-2020-102
Preprint. Discussion started: 24 June 2020
© Author(s) 2020. CC BY 4.0 License.

Table 1. Overview over the SOCOL simulations and the microphysical parameter settings.

Parameter	n_{ice}	$n_{\text{NAT,max}}$	r_{NAT}
S_{REF}	0.01 cm^{-3}	5x10^{-4} cm^{-3}	5 μm
$S_{n(ice)}$	**0.1 cm^{-3}**	5x10^{-4} cm^{-3}	5 μm
$S_{n(NAT,max)}$	0.01 cm^{-3}	**2x10^{-3} cm^{-3}**	5 μm
$S_{n(ice),n(NAT,max)}$	**0.05 cm^{-3}**	**1x10^{-3} cm^{-3}**	5 μm

3.4 Sensitivity to microphysical parameters

As described in Sect. 2.1 SOCOL's PSC scheme includes some prescribed microphysical parameters such as the ice particle number density, n_{ice}, or the NAT radius, r_{NAT}. These values had once been chosen based on what was known about PSCs back then. However, the current parameter setting might not be optimal. For example, the rather low value for n_{ice} of 0.01 cm^{-3} prevents the formation of ice PSCs with high number densities as observed in mountain wave events. To investigate the sensitivity of the simulated PSCs to the microphysical parameters in the PSC scheme, we performed additional simulations for the Antarctic winter 2007 with increased n_{ice} and/or increased $n_{\text{NAT,max}}$ (Table 1).

Figure 6 shows the composite histograms for the various SOCOL simulations. There are considerable differences to the observations (Fig. 1), but also between the simulations. PSCs in the REF simulation show a strong relative maximum located in the STS domain with $1/R_{532}$ values between 0.4 and 0.2 (Fig. 6a). Only very few PSCs are classified as ice, i.e. the relative maximum towards the upper right, as observed by CALIPSO, is missing. That the PSC mixtures in the simulations are located more at the lower and left side of the histogram can also be seen in Fig. 2c. There are several reasons for this difference. First, SOCOL does not resolve mountain waves due to the coarse model resolution and orography. Furthermore, the modeled PSCs are representative for large grid box (2.8°x2.8°horizontally and approximately 2 km vertically), while the observations resolve much smaller scale structures (starting from 5 km horizontally along a track and 180 m vertically). Finally, the fixed ice number density of 0.01 cm^{-3} does not allow for large ice particle cross sections, even if mountain waves would be resolved. Based on these findings we performed one sensitivity simulation with a tenfold ice number density, $S_{n(ice)}$. As shown Fig. 6b the tenfold increase in n_{ice} results in a strong maximum to the upper right, mainly within the enhanced NAT mixture domain. The higher number density of ice particles increases the cross section of ice, leading to enhanced backscatter in ice-containing grid cells. Due to its solid state, backscatter from ice has δ_{aerosol}>0. This results in a shift towards higher R_{532} and higher δ_{aerosol} values in the histogram. Overall, modifying n_{ice} leads to a better agreement with CALIPSO.

While ice PSCs are less important for stratospheric ozone chemistry, NAT formation and subsequent denitrification of the stratosphere play a crucial role. NAT formation in SOCOL depends on two parameters, $n_{\text{NAT,max}}$ and r_{NAT}. To test the model's sensitivity to those parameters, we ran further simulations with the upper boundary for NAT number densities increased by a

https://doi.org/10.5194/gmd-2020-102
Preprint. Discussion started: 24 June 2020
© Author(s) 2020. CC BY 4.0 License.

factor of four, $S_{n(NAT,max)}$, and the NAT radius increased from 5 to 7 µm. As both simulations showed similar changes, the latter is not presented here.

The simulation with four times higher $n_{\text{NAT,max}}$ (Fig. 6c) shows a maximum shifted towards lower R_{532} values compared to the REF simulation, which is located around the optical thresholds at the lower left corner. As long as temperatures are below T_{NAT} and enough HNO_3 is available for NAT formation, an increase in $n_{\text{NAT,max}}$ or r_{NAT} results in more HNO_3-uptake by NAT particles. This reduces the available gas-phase HNO_3 for STS growth. Also, more HNO_3 through sedimentation of the solid NAT particles is removed. With larger r_{NAT} this removal occurs even faster due to the higher sedimentation velocity. The reduction in surface area density of STS results in less backscatter and subsequently a shift towards lower R_{532} values in the composite histogram. This shift towards lower R_{532} values worsens agreement with observations.

In a final simulation ($S_{n(ice),n(NAT,max)}$, Fig. 6d) we set n_{ice} to 0.05 cm^{-3} and $n_{\text{NAT,max}}$ to 10^{-3} cm^{-3}. This simulation shows a superposition of the two effects described above, resulting in two distinct relative maxima in the composite histogram. One maxima is located to the upper right, similar to $S_{n(ice)}$. The second maximum at low R_{532} and low δ_{aerosol} values is similar to the pattern in $S_{n(NAT,max)}$. The shift towards lower R_{532} values is again a result of less STS formation due to the reduced availability of HNO_3. Although the composition histograms of all sensitivity simulations differ substantially from observations, we find the best agreement for the simulation $S_{n(ice),n(NAT,max)}$.

To investigate the impact of the applied modifications on the simulated chemical composition of the polar stratosphere (60–82°S), we compare modeled gas-phase HNO_3, H_2O and O_3 with MLS measurements for 46 and 68 hPa (Figs. 7 - 9). To account for the spatial heterogeneity of the MLS measurements, we calculated area-weighted concentrations for the SOCOL grid boxes. The top panels shows absolute values for MLS the REF simulation, while the lower panels show the temporal evolution relative to 01 May.

At the beginning of winter, all simulations have similar HNO_3 concentrations, which are about 20% to 100% lower than MLS, depending on the pressure level. At 46 hPa MLS HNO_3 starts to decline around mid-May and in early June at 68 hPa. Prior to the decline, an increase in HNO_3 is observed at 68 hPa. It results from the evaporation of sedimenting NAT particles formed at higher altitudes (renitrification) and is an indication of denitrification of the upper levels. During July/August the absolute HNO_3 values from the reference run agree well with the observations. However, in late winter SOCOL again underestimates MLS. All simulations show a decline due to HNO_3-uptake into NAT particles and STS droplets. However, S_{REF} (black) and $S_{n(ice)}$ (cyan) show a weaker and delayed HNO_3 decline with a plateau in July/August.

In $S_{n(NAT,max)}$ (green) the decline at both levels is considerably stronger than in S_{REF} as well as in MLS. This is due to the enhanced uptake of HNO_3 into NAT particles and the subsequent removal by sedimentation. As a consequence also the renitrification at lower levels is clearly enhanced. Both indicates a more efficient denitrification than in S_{REF}.

The simulation $S_{n(ice),n(NAT,max)}$ (red), in which $n_{\text{NAT,max}}$ is twice as large as in S_{REF}, but only half of $S_{n(NAT,max)}$, falls in between the other simulations. The denitrification starts about half a month later than in $S_{n(NAT,max)}$. The HNO_3-uptake is reduced and subsequently HNO_3 stays longer in the gas-phase. However, in August HNO_3 concentrations reach about the same level as in $S_{n(NAT,max)}$. Simulations with enhanced r_{NAT} have similar effects (not shown).

https://doi.org/10.5194/gmd-2020-102
Preprint. Discussion started: 24 June 2020
© Author(s) 2020. CC BY 4.0 License.

Geoscientific Model Development
Discussions
Open Access
EGU

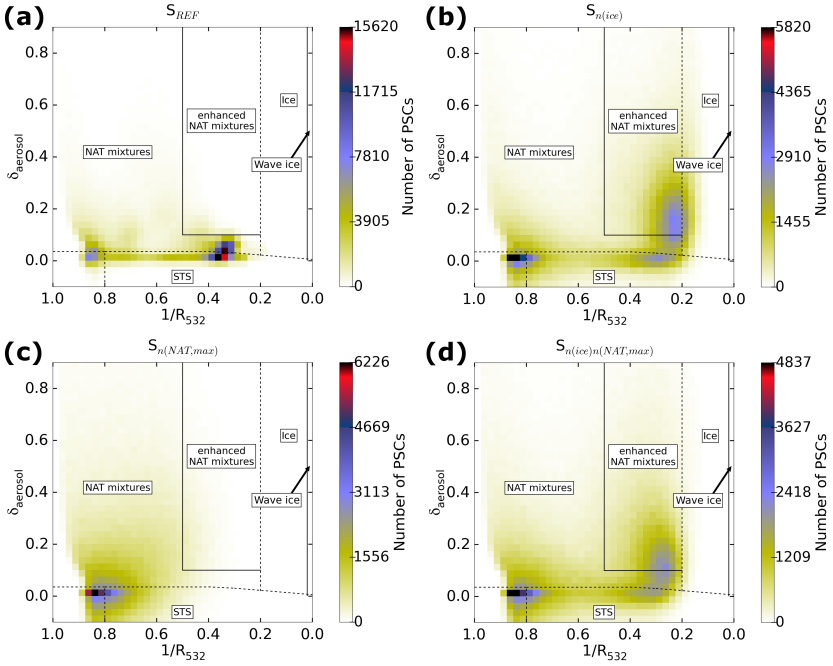

Figure 6. Composite 2D-histograms for July 2007, analogue to Fig. 1, for the simulations S_{REF} (a), $S_{n(ice)}$ (b), $S_{n(NAT,max)}$ (c) and $S_{n(ice),n(NAT,max)}$ (d).

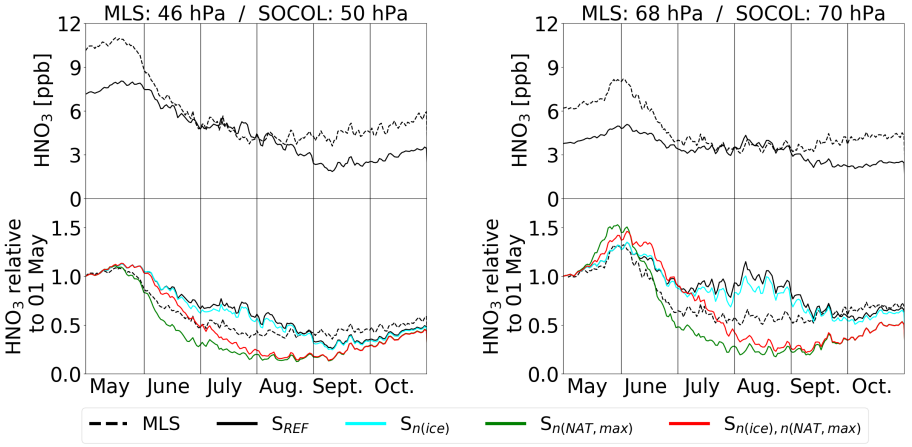

Figure 7. Temporal evolution of polar (60°S-82°S) mean gas-phase HNO_3 from MLS measurements and the different model simulations.

https://doi.org/10.5194/gmd-2020-102
Preprint. Discussion started: 24 June 2020
© Author(s) 2020. CC BY 4.0 License.

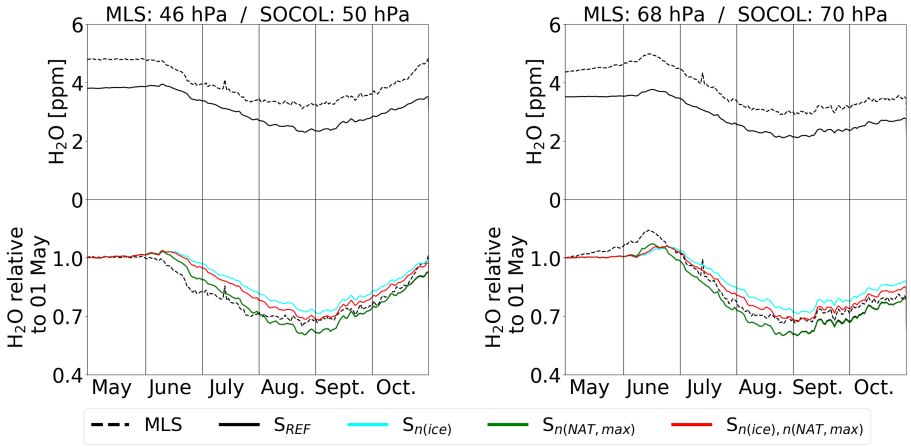

Figure 8. Same as Fig. 7, but for H_2O. Note that the line of $S_{n(NAT,max)}$ overlays S_{REF}, since these simulations have identical H_2O.

Figure 8 shows the same as Fig. 7, but for H_2O. As for HNO_3, all simulations start with similar H_2O values in May, but underestimate MLS by 20% to 30%. At 46 hPa MLS H_2O starts to decline beginning of June. Rehydration of lower levels due to the evaporation of sedimenting ice particles is observed shortly after. At 68 hPa, MLS H_2O starts to decrease mid of June. All model simulations show a very similar temporal evolution of H_2O in the polar stratosphere and a very good agreement with MLS. In SOCOL the amount of ice is determined by the amount of available H_2O and temperatures. The smaller the chosen n_{ice}, the larger the ice particles and the stronger the dehydration due to faster sedimentation. S_{REF} and $S_{n(NAT,max)}$, the simulations with the lowest n_{ice} of 0.01 cm^{-3}, show the strongest dehydration and the earliest onset, while $S_{n(ice)}$ with n_{ice}=0.1 cm^{-3} shows the smallest dehydration.

Finally, Fig. 9 presents simulated O_3 in the polar stratosphere compared to MLS. At the beginning of winter all model simulations are in very good agreement with MLS measurements. For both pressure levels, the simulations show an earlier and stronger decline in O_3 than observed by MLS. Also, the recovery of O_3 starts earlier, leading to slightly higher O_3 values at the end of October. The spread among the model simulations is small compared to the differences to the observations. Increasing the parameter n_{ice} affects the modeled stratospheric composition only very little by reducing dehydration. But the increased SAD of ice leads to slightly lower O_3 in $S_{n(ice)}$ compared to S_{REF}. Increasing the upper NAT boundary overall reduces SAD of PSC due to reducing the abundance of HNO_3. However, due to enhanced denitrification, $S_{n(NAT,max)}$ and $S_{n(ice),n(NAT,max)}$ show even slightly lower O_3 concentrations.

4 Conclusions

We have presented an evaluation of PSCs as simulated by the CCM SOCOLv3.1 in specified dynamics mode for the Antarctic winter 2007. SOCOL considers STS droplets as well as water ice and NAT particles. PSCs are parametrized in terms of tem-

https://doi.org/10.5194/gmd-2020-102
Preprint. Discussion started: 24 June 2020
© Author(s) 2020. CC BY 4.0 License.

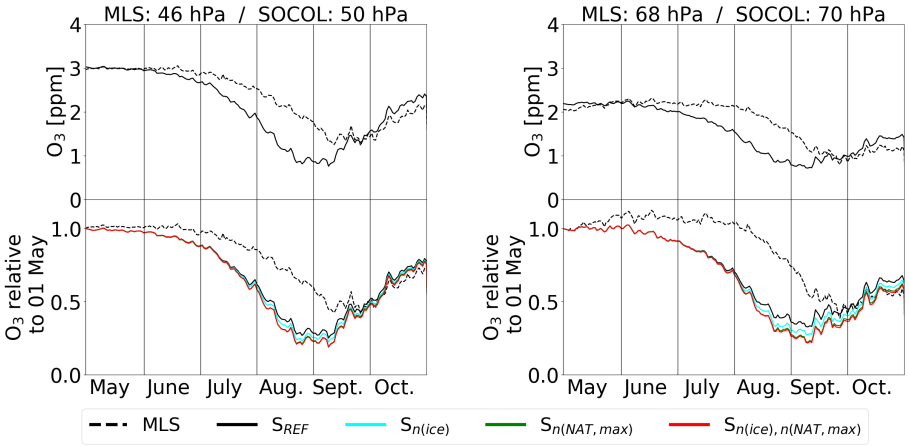

Figure 9. Same as Fig. 7, but for O_3.

perature and partial pressures of HNO_3 and H_2O, assuming equilibrium conditions. The PSCs scheme includes several fixed microphysical parameters, namely the maximum NAT number density, NAT radius and ice number density. PSC occurrence and composition have been compared to CALIPSO/CALIOP satellite observations by mimicking a lidar measurement on the model output. The impact of PSCs on the chemical composition of the polar stratosphere has been investigated by comparison with Aura/MLS data.

Overall, the spatial agreement with CALIOP observations is good and the observed month-to-month variability is represented. However, due to the coarse model, mean orography, but also the fixed ice number densities, mountain wave events and associated wave ice clouds with high backscatter ratios over the Antarctic Peninsula are not resolved in SOCOL. The temporal and spatial evolution of PSCs inside the polar vortex as expressed by the areal coverage indicates an overestimation of PSCs in SOCOL. This is partly explained by a cold temperature bias, but also by the coarse model resolution: even a small amount of PSCs within a grid cell adds a large contribution to the areal coverage. This is reflected by the sensitivity of this quantity towards the applied detection thresholds.

Furthermore, we have tested the assumptions about the maximum NAT number density, NAT radius and ice number density by various sensitivity simulations. The parameter n_{ice} determines primarily the optical signal through its impact on the particle cross section and also dehydration due to changing settling velocities with changing particle radius. While increasing n_{ice} from $0.01\ \mathrm{cm}^{-3}$ to $0.1\ \mathrm{cm}^{-3}$ improves the agreement of the optical signal with CALIOP, the simulated dehydration is more realistic for smaller n_{ice} and therefore larger ice particles.

The upper boundary for NAT number densities determines the HNO_3-uptake and subsequently the magnitude of STS formation, which is crucial for halogen activation. We have shown that for an increased max. NAT number densities the temporal agreement of de- and renitrification with MLS measurements is improved. However, SOCOL in general clearly underestimates observed HNO_3 in the polar stratosphere, which makes a solid conclusion about the best set of microphysical parameters

https://doi.org/10.5194/gmd-2020-102
Preprint. Discussion started: 24 June 2020
© Author(s) 2020. CC BY 4.0 License.

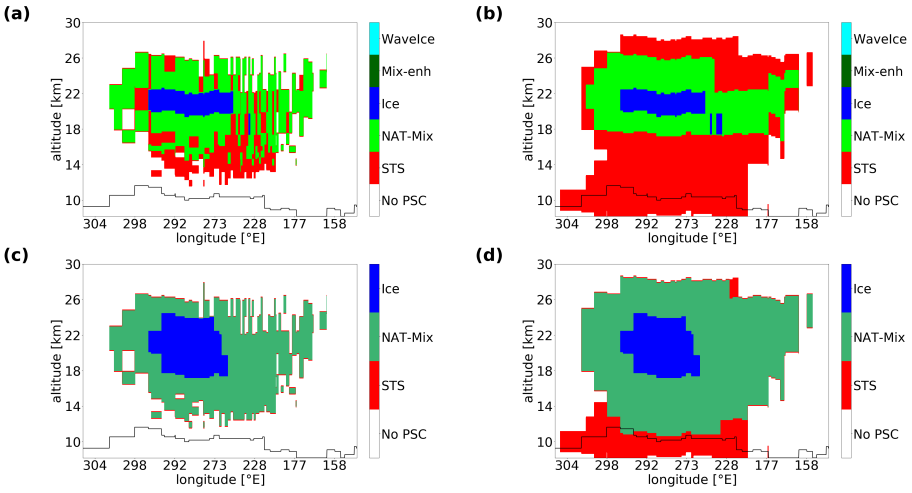

Figure A1. Panels a) and b) show the composition according to the classification scheme in Pitts et al. (2018) of the modeled PSCs for the 1st July 2007 case in the CALIOP orbit from Fig. 3b and c. Panels c) and d) show the modeled PSC composition.

difficult. Despite stratospheric H_2O and in particular HNO_3 being very sensitive to the microphysical parameter settings, the impact on O_3 is very small. Best overall agreement with the CALIOP and MLS measurements is found for this case study with the NAT and ice number concentrations increased from their default values to n_{ice}=0.05 cm^{-3} and $n_{\mathrm{NAT,max}}$=$1{\cdot}10^{-3}$ cm^{-3}, respectively. Further work would be required to extend our findings to simulated PSCs in the Arctic or to other years. Nevertheless, this study demonstrates that also a simplified PSC scheme based on equilibrium assumptions may achieve good approximations of fundamental properties of polar stratospheric clouds needed in chemistry-climate models.

Code and data availability. Since the full SOCOLv3.1 code is based on ECHAM5, users must first sign the ECHAM5 license agreement before accessing the SOCOLv3.1 code (http://www.mpimet.mpg.de/en/science/models/license/, last access: 2020). The SOCOLv3.1 code is then freely available upon request from Andrea Stenke (andrea.stenke@env.ethz.ch). The source code of the PSC module as well as the Mie and T-matrix scattering code are available at https://doi.org/10.5281/zenodo.3726766. The simulation data presented in this paper can be downloaded from the ETH Research Collection via http://dx.doi.org/10.3929/ethz-b-000406548. CALIPSO lidar level 2 polar stratospheric cloud mask version 2.0 (v2) is available on request to Michael C. Pitts. MLS HNO_3, H_2O and O_3 data products have been downloaded from https://mls.jpl.nasa.gov/index-eos-mls.php (latest access 01.11.2018).

Author contributions. AS and TP initiated the project of evaluating the PSC parametrization in SOCOL. AS conducted all SOCOL simulations. BL provided the Mie and T-matrix scattering code. MS analyzed the model results and wrote the paper. MP provided the CALIOP v2 data. All coauthors helped with the interpretation of the data and contributed to the manuscript.

https://doi.org/10.5194/gmd-2020-102
Preprint. Discussion started: 24 June 2020
© Author(s) 2020. CC BY 4.0 License.

Geoscientific Model Development Discussions
Open Access

Competing interests. The authors declare that they have no conflict of interest.

Acknowledgements. Special thanks go to Beiping Luo for providing the Mie and T-matrix scattering code. We thank Aryeh Feinberg and Franziska Zilker for their technical assistance and support. We also gratefully acknowledge Lamont Poole at NASA Langley Research Center for his help with the CALIPSO figures.

https://doi.org/10.5194/gmd-2020-102
Preprint. Discussion started: 24 June 2020
© Author(s) 2020. CC BY 4.0 License.

References

Akiyoshi, H., Zhou, L. B., Yamashita, Y., Sakamoto, K., Yoshiki, M., Nagashima, T., Takahashi, M., Kurokawa, J., Takigawa, M., and Imamura, T.: A CCM simulation of the breakup of the Antarctic polar vortex in the years 1980-2004 under the CCMVal scenarios, J. Geophys. Res., 114, https://doi.org/10.1029/2007jd009261, 2009.

Bardeen, C. G., Gettelman, A., Jensen, E. J., Heymsfield, A., Conley, A. J., Delanoe, J., Deng, M., and Toon, O. B.: Improved cirrus simulations in a general circulation model using CARMA sectional microphysics, J. Geophys. Res., 118, 11 679–11 697, https://doi.org/10.1002/2013jd020193, 2013.

Biele, J., Tsias, A., Luo, B. P., Carslaw, K. S., Neuber, R., Beyerle, G., and Peter, T.: Nonequilibrium coexistence of solid and liquid particles in Arctic stratospheric clouds, J. Geophys. Res., 106, 22 991–23 007, https://doi.org/10.1029/2001jd900188, 2001.

Carslaw, K. S., Luo, B. P., and Peter, T.: An analytic expression for the composition of aqueous $HNO_3-H_2SO_4$ stratospheric aerosols including gas-phase removal of HNO_3, Geophys. Res. Lett., 22, 1877–1880, https://doi.org/10.1029/95gl01668, 1995.

Daerden, F., Larsen, N., Chabrillat, S., Errera, Q., Bonjean, S., Fonteyn, D., Hoppel, K., and Fromm, M.: A 3D-CTM with detailed online PSC-microphysics: analysis of the Antarctic winter 2003 by comparison with satellite observations, Atmos. Chem. Phys., 7, 1755–1772, https://doi.org/10.5194/acp-7-1755-2007, 2007.

Dee, D. P., Uppala, S. M., Simmons, A. J., Berrisford, P., Poli, P., Kobayashi, S., Andrae, U., Balmaseda, M. A., Balsamo, G., Bauer, P., Bechtold, P., Beljaars, A. C. M., van de Berg, L., Bidlot, J., Bormann, N., Delsol, C., Dragani, R., Fuentes, M., Geer, A. J., Haimberger, L., Healy, S. B., Hersbach, H., Holm, E. V., Isaksen, L., Kallberg, P., Kohler, M., Matricardi, M., McNally, A. P., Monge-Sanz, B. M., Morcrette, J. J., Park, B. K., Peubey, C., de Rosnay, P., Tavolato, C., Thepaut, J. N., and Vitart, F.: The ERA-Interim reanalysis: configuration and performance of the data assimilation system, Q. J. R. Meteorol. Soc., 137, 553–597, https://doi.org/10.1002/qj.828, 2011.

Egorova, T. A., Rozanov, E. V., Zubov, V. A., and Karol, I. L.: Model for investigating ozone trends (MEZON), Izv. Atmos. Ocean. Phys., 39, 277–292, 2003.

Engel, I., Luo, B. P., Pitts, M. C., Poole, L. R., Hoyle, C. R., Grooß, J.-U., Dörnbrack, A., and Peter, T.: Heterogeneous formation of polar stratospheric clouds - Part 2: Nucleation of ice on synoptic scales, Atmos. Chem. Phys., 13, 10 769–10 785, https://doi.org/10.5194/acp-13-10769-2013, 2013.

Fahey, D. W., Gao, R. S., Carslaw, K. S., Kettleborough, J., Popp, P. J., Northway, M. J., Holecek, J. C., Ciciora, S. C., McLaughlin, R. J., Thompson, T. L., Winkler, R. H., Baumgardner, D. G., Gandrud, B., Wennberg, P. O., Dhaniyala, S., McKinney, K., Peter, T., Salawitch, R. J., Bui, T. P., Elkins, J. W., Webster, C. R., Atlas, E. L., Jost, H., Wilson, J. C., Herman, R. L., Kleinböhl, A., and von König, M.: The detection of large HNO_3-containing particles in the winter arctic stratosphere, Science, 291, 1026–1031, https://doi.org/10.1126/science.1057265, 2001.

Farman, J. C., Gardiner, B. G., and Shanklin, J. D.: Large losses of total ozone in Antarctica reveal seasonal $ClOx/NOx$ interaction, Nature, 315, 207–210, https://doi.org/10.1038/315207a0, 1985.

Feng, W., Chipperfield, M. P., Davies, S., Mann, G. W., Carslaw, K. S., Dhomse, S., Harvey, L., Randall, C., and Santee, M. L.: Modelling the effect of denitrification on polar ozone depletion for Arctic winter 2004/2005, Atmos. Chem. Phys., 11, 6559–6573, https://doi.org/10.5194/acp-11-6559-2011, 2011.

Fischer, H. and Oelhaf, H.: Remote sensing of vertical profiles of atmospheric trace constituents with MIPAS limb-emission spectrometers, Appl. Opt., 35, 2787–2796, https://doi.org/10.1364/Ao.35.002787, 1996.

Fischer, H., Birk, M., Blom, C., Carli, B., Carlotti, M., von Clarmann, T., Delbouille, L., Dudhia, A., Ehhalt, D., Endemann, M., Flaud, J. M., Gessner, R., Kleinert, A., Koopman, R., Langen, J., Lopez-Puertas, M., Mosner, P., Nett, H., Oelhaf, H., Perron, G., Remedios, J., Ridolfi, M., Stiller, G., and Zander, R.: MIPAS: an instrument for atmospheric and climate research, Atmos. Chem. Phys., 8, 2151–2188, https://doi.org/10.5194/acp-8-2151-2008, 2008.

Garcia, R. R., Marsh, D. R., Kinnison, D. E., Boville, B. A., and Sassi, F.: Simulation of secular trends in the middle atmosphere, 1950-2003, J. Geophys. Res., 112, https://doi.org/10.1029/2006jd007485, 2007.

Garcia, R. R., Smith, A. K., Kinnison, D. E., de la Camara, A., and Murphy, D. J.: Modification of the Gravity Wave Parameterization in the Whole Atmosphere Community Climate Model: Motivation and Results, Journal of the Atmospheric Sciences, 74, 275–291, https://doi.org/10.1175/Jas-D-16-0104.1, <GotoISI>://WOS:000392419300016, 2017.

Gelaro, R., McCarty, W., Suarez, M. J., Todling, R., Molod, A., Takacs, L., Randles, C. A., Darmenov, A., Bosilovich, M. G., Reichle, R., Wargan, K., Coy, L., Cullather, R., Draper, C., Akella, S., Buchard, V., Conaty, A., da Silva, A. M., Gu, W., Kim, G. K., Koster, R., Lucchesi, R., Merkova, D., Nielsen, J. E., Partyka, G., Pawson, S., Putman, W., Rienecker, M., Schubert, S. D., Sienkiewicz, M., and Zhao, B.: The Modern-Era Retrospective Analysis for Research and Applications, Version 2 (MERRA-2), J. Clim., 30, 5419–5454, https://doi.org/10.1175/Jcli-D-16-0758.1, 2017.

Grooß, J.-U., Tritscher, I., and Chipperfield, M. P.: Polar Stratospheric Clouds in Global Models, in preparation, 2020.

Hanson, D. and Mauersberger, K.: Laboratory studies of the nitric-acid trihydrate - implications for the south polar stratosphere, Geophys. Res. Lett., 15, 855–858, https://doi.org/10.1029/GL015i008p00855, 1988.

Hoffmann, L., Spang, R., Orr, A., Alexander, M. J., Holt, L. A., and Stein, O.: A decadal satellite record of gravity wave activity in the lower stratosphere to study polar stratospheric cloud formation, Atmos. Chem. Phys., 17, 2901–2920, https://doi.org/10.5194/acp-17-2901-2017, 2017.

Höpfner, M., Larsen, N., Spang, R., Luo, B. P., Ma, J., Svendsen, S. H., Eckermann, S. D., Knudsen, B., Massoli, P., Cairo, F., Stiller, G., von Clarmann, T., and Fischer, H.: MIPAS detects Antarctic stratospheric belt of NAT PSCs caused by mountain waves, Atmos. Chem. Phys., 6, 1221–1230, https://doi.org/10.5194/acp-6-1221-2006, 2006.

Hostetler, C., Liu, Z., Reagan, J., Vaughan, M., Winker, D., Osborn, M., Hunt, W., Powell, K., and Trepte, C.: Calibration and Level 1 Data Products, https://www-calipso.larc.nasa.gov/resources/pdfs/PC-SCI-201v1.0.pdf, 2006.

Hoyle, C. R., Engel, I., Luo, B. P., Pitts, M. C., Poole, L. R., Grooß, J.-U., and Peter, T.: Heterogeneous formation of polar stratospheric clouds - Part 1: Nucleation of nitric acid trihydrate (NAT), Atmos. Chem. Phys., 13, 9577–9595, https://doi.org/10.5194/acp-13-9577-2013, 2013.

Hu, R. M., Carslaw, K. S., Hostetler, C., Poole, L. R., Luo, B. P., Peter, T., Fueglistaler, S., McGee, T. J., and Burris, J. F.: Microphysical properties of wave polar stratospheric clouds retrieved from lidar measurements during SOLVE/THESEO 2000, J. Geophys. Res., 107, https://doi.org/10.1029/2001jd001125, 2002.

Jiang, Y. B., Froidevaux, L., Lambert, A., Livesey, N. J., Read, W. G., Waters, J. W., Bojkov, B., Leblanc, T., McDermid, I. S., Godin-Beekmann, S., Filipiak, M. J., Harwood, R. S., Fuller, R. A., Daffer, W. H., Drouin, B. J., Cofield, R. E., Cuddy, D. T., Jarnot, R. F., Knosp, B. W., Perun, V. S., Schwartz, M. J., Snyder, W. V., Stek, P. C., Thurstans, R. P., Wagner, P. A., Allaart, M., Andersen, S. B., Bodeker, G., Calpini, B., Claude, H., Coetzee, G., Davies, J., De Backer, H., Dier, H., Fujiwara, M., Johnson, B., Kelder, H., Leme, N. P., Konig-Langlo, G., Kyro, E., Laneve, G., Fook, L. S., Merrill, J., Morris, G., Newchurch, M., Oltmans, S., Parrondos, M. C., Posny, F., Schmidlin, F., Skrivankova, P., Stubi, R., Tarasick, D., Thompson, A., Thouret, V., Viatte, P., Vömel, H., von der Gathen, P., Yela, M., and Zablocki, G.: Validation of Aura Microwave Limb Sounder ozone by ozonesonde and lidar measurements, J. Geophys. Res., 112, https://doi.org/10.1029/2007jd008776, 2007.

Jourdain, L., Bekki, S., Lott, F., and Lefevre, F.: The coupled chemistry-climate model LMDz-REPROBUS: description and evaluation of a transient simulation of the period 1980-1999, Ann. Geophys., 26, 1391–1413, https://doi.org/10.5194/angeo-26-1391-2008, 2008.

Khosrawi, F., Kirner, O., Stiller, G., Höpfner, M., Santee, M. L., Kellmann, S., and Braesicke, P.: Comparison of ECHAM5/MESSy Atmospheric Chemistry (EMAC) simulations of the Arctic winter 2009/2010 and 2010/2011 with Envisat/MIPAS and Aura/MLS observations, Atmos. Chem. Phys., 18, 8873–8892, https://doi.org/10.5194/acp-18-8873-2018, 2018.

Kirner, O., Müller, R., Ruhnke, R., and Fischer, H.: Contribution of liquid, NAT and ice particles to chlorine activation and ozone depletion in Antarctic winter and spring, Atmos. Chem. Phys., 15, 2019–2030, https://doi.org/10.5194/acp-15-2019-2015, 2015.

Lambert, A., Read, W. G., Livesey, N. J., Santee, M. L., Manney, G. L., Froidevaux, L., Wu, D. L., Schwartz, M. J., Pumphrey, H. C., Jimenez, C., Nedoluha, G. E., Cofield, R. E., Cuddy, D. T., Daffer, W. H., Drouin, B. J., Fuller, R. A., Jarnot, R. F., Knosp, B. W., Pickett, H. M., Perun, V. S., Snyder, W. V., Stek, P. C., Thurstans, R. P., Wagner, P. A., Waters, J. W., Jucks, K. W., Toon, G. C., Stachnik, R. A., Bernath, P. F., Boone, C. D., Walker, K. A., Urban, J., Murtagh, D., Elkins, J. W., and Atlas, E.: Validation of the Aura Microwave Limb Sounder middle atmosphere water vapor and nitrous oxide measurements, J. Geophys. Res., 112, https://doi.org/10.1029/2007jd008724, 2007.

Livesey, N. J., Read, W. G., Wagner, P. A., Froidevaux, L., Lambert, A., Manney, G. L., Millán Valle, L. F., Pumphrey, H. C., Santee, M. L., Schwartz, M. J., Wang, S., Fuller, R. A., Jarnot, R. F., Knosp, B. W., Martinez, E., and Lay, R. R.: Earth Observing System (EOS), Aura Microwave Limb Sounder (MLS), Version 4.2 Level 2 data quality and description document, https://mls.jpl.nasa.gov/data/v4-2_data_quality_document.pdf, 2018.

Mishchenko, M. I., Travis, L. D., and Mackowski, D. W.: T-Matrix computations of light scattering by nonspherical particles: A review, J. Quant. Spectrosc. Radiat. Transf., 55, 535–575, https://doi.org/10.1016/0022-4073(96)00002-7, 1996.

Molina, L. T. and Molina, M. J.: Production of Cl_2O_2 from the self-reaction of the ClO radical, J. Phys. Chem., 91, 433–436, https://doi.org/10.1021/j100286a035, 1987.

Morgenstern, O., Hegglin, M. I., Rozanov, E., O'Connor, F. M., Abraham, N. L., Akiyoshi, H., Archibald, A. T., Bekki, S., Butchart, N., Chipperfield, M. P., Deushi, M., Dhomse, S. S., Garcia, R. R., Hardiman, S. C., Horowitz, L. W., Jöckel, P., Josse, B., Kinnison, D., Lin, M. Y., Mancini, E., Manyin, M. E., Marchand, M., Marecal, V., Michou, M., Oman, L. D., Pitari, G., Plummer, D. A., Revell, L., Saint-Martin, D., Schofield, R., Stenke, A., Stone, K., Sudo, K., Tanaka, T. Y., Tilmes, S., Yamashita, Y., Yoshida, K., and Zeng, G.: Review of the global models used within phase 1 of the Chemistry-Climate Model Initiative (CCMI), Geosc. Model Dev., 10, 639–671, https://doi.org/10.5194/gmd-10-639-2017, 2017.

Pitts, M. C., Poole, L. R., and Gonzalez, R.: Polar stratospheric cloud climatology based on CALIPSO spaceborne lidar measurements from 2006 to 2017, Atmos. Chem. Phys., 18, 10 881–10 913, https://doi.org/10.5194/acp-18-10881-2018, 2018.

Portmann, R., Solomon, S., Garcia, R., Thomason, L., Poole, L., and McCormick, M.: Role of aerosol variations in anthropogenic ozone depletion in the polar regions, Journal of Geophysical Research Atmospheres, 101, 22 991–23 006, 1996.

Pöschl, U., von Kuhlmann, R., Poisson, N., and Crutzen, P. J.: Development and intercomparison of condensed isoprene oxidation mechanisms for global atmospheric modeling, J. Atmos. Chem., 37, 29–52, https://doi.org/10.1023/A:1006391009798, 2000.

Pruppacher, H. R. and Klett, J. D.: Microphysics of clouds and precipitation, Springer, https://doi.org/10.1007/978-0-306-48100-0, 1997.

Read, W. G., Lambert, A., Bacmeister, J., Cofield, R. E., Christensen, L. E., Cuddy, D. T., Daffer, W. H., Drouin, B. J., Fetzer, E., Froidevaux, L., Fuller, R., Herman, R., Jarnot, R. F., Jiang, J. H., Jiang, Y. B., Kelly, K., Knosp, B. W., Kovalenko, L. J., Livesey, N. J., Liu, H. C., Manney, G. L., Pickett, H. M., Pumphrey, H. C., Rosenlof, K. H., Sabounchi, X., Santee, M. L., Schwartz, M. J., Snyder, W. V., Stek, P. C., Su, H., Takacs, L. L., Thurstans, R. P., Vömel, H., Wagner, P. A., Waters, J. W., Webster, C. R., Weinstock, E. M., and Wu, D. L.:

Aura Microwave Limb Sounder upper tropospheric and lower stratospheric H_2O and relative humidity with respect to ice validation, J. Geophys. Res., 112, https://doi.org/10.1029/2007jd008752, 2007.

Revell, L. E., Tummon, F., Stenke, A., Sukhodolov, T., Coulon, A., Rozanov, E., Garny, H., Grewe, V., and Peter, T.: Drivers of the tropospheric ozone budget throughout the 21st century under the medium-high climate scenario RCP 6.0, Atmos. Chem. Phys., 15, 5887–5902, https://doi.org/10.5194/acp-15-5887-2015, 2015.

Roeckner, E., Brokopf, R., Esch, M., Giorgetta, M., Hagemann, S., Kornblueh, L., Manzini, E., Schlese, U., and Schulzweida, U.: Sensitivity of simulated climate to horizontal and vertical resolution in the ECHAM5 atmosphere model, J. Clim., 19, 3771–3791, https://doi.org/10.1175/Jcli3824.1, 2006.

Salawitch, R. J., Wofsy, S. C., Gottlieb, E. W., Lait, L. R., Newman, P. A., Schoeberl, M. R., Loewenstein, M., Podolske, J. R., Strahan, S. E., Proffitt, M. H., Webster, C. R., May, R. D., Fahey, D. W., Baumgardner, D., Dye, J. E., Wilson, J. C., Kelly, K. K., Elkins, J. W., Chan, K. R., and Anderson, J. G.: Chemical loss of ozone in the Arctic polar vortex in the winter of 1991-1992, Science, 261, 1146–1149, https://doi.org/10.1126/science.261.5125.1146, 1993.

Santee, M. L., Lambert, A., Read, W. G., Livesey, N. J., Cofield, R. E., Cuddy, D. T., Daffer, W. H., Drouin, B. J., Froidevaux, L., Fuller, R. A., Jarnot, R. F., Knosp, B. W., Manney, G. L., Perun, V. S., Snyder, W. V., Stek, P. C., Thurstans, R. P., Wagner, P. A., Waters, J. W., Muscari, G., de Zafra, R. L., Dibb, J. E., Fahey, D. W., Popp, P. J., Marcy, T. P., Jucks, K. W., Toon, G. C., Stachnik, R. A., Bernath, P. F., Boone, C. D., Walker, K. A., Urban, J., and Murtagh, D.: Validation of the Aura Microwave Limb Sounder HNO_3 measurements, J. Geophys. Res., 112, https://doi.org/10.1029/2007jd008721, 2007.

Schoeberl, M. R.: The EOS Aura Mission, pp. 64–70, Springer, New York, NY, https://doi.org/10.1007/978-0-387-35848-2_4, 2007.

Simpson, S., Chu, X., Liu, A., Robinson, W., Nott, G., Diettrich, J., Espy, P., and Shanklin, J.: Polar stratospheric clouds observed by a lidar at Rothera, Antarctica (67.5°S, 68.0°W), Proc. SPIE, 5887, https://doi.org/10.1117/12.620399, 2005.

Snels, M., Scoccione, A., Di Liberto, L., Colao, F., Pitts, M., Poole, L., Deshler, T., Cairo, F., Cagnazzo, C., and Fierli, F.: Comparison of Antarctic polar stratospheric cloud observations by ground-based and space-borne lidar and relevance for chemistry-climate models, Atmos. Chem. Phys., 19, 955–972, https://doi.org/10.5194/acp-19-955-2019, 2019.

Solomon, S., Garcia, R. R., Rowland, F. S., and Wuebbles, D. J.: On the depletion of Antarctic ozone, Nature, 321, 755–758, https://doi.org/10.1038/321755a0, 1986.

Stenke, A., Schraner, M., Rozanov, E., Egorova, T., Luo, B., and Peter, T.: The SOCOL version 3.0 chemistry-climate model: description, evaluation, and implications from an advanced transport algorithm, Geosc. Model Dev., 6, 1407–1427, https://doi.org/10.5194/gmd-6-1407-2013, 2013.

Tritscher, I., Grooß, J.-U., Spang, R., Pitts, M. C., Poole, L. R., Müller, R., and Riese, M.: Lagrangian simulation of ice particles and resulting dehydration in the polar winter stratosphere, Atmos. Chem. Phys., 19, 543–563, https://doi.org/10.5194/acp-19-543-2019, 2019.

Waters, J. W., Froidevaux, L., Harwood, R. S., Jarnot, R. F., Pickett, H. M., Read, W. G., Siegel, P. H., Cofield, R. E., Filipiak, M. J., Flower, D. A., Holden, J. R., Lau, G. K. K., Livesey, N. J., Manney, G. L., Pumphrey, H. C., Santee, M. L., Wu, D. L., Cuddy, D. T., Lay, R. R., Loo, M. S., Perun, V. S., Schwartz, M. J., Stek, P. C., Thurstans, R. P., Boyles, M. A., Chandra, K. M., Chavez, M. C., Chen, G. S., Chudasama, B. V., Dodge, R., Fuller, R. A., Girard, M. A., Jiang, J. H., Jiang, Y. B., Knosp, B. W., LaBelle, R. C., Lam, J. C., Lee, K. A., Miller, D., Oswald, J. E., Patel, N. C., Pukala, D. M., Quintero, O., Scaff, D. M., Van Snyder, W., Tope, M. C., Wagner, P. A., and Walch, M. J.: The Earth Observing System Microwave Limb Sounder (EOS MLS) on the Aura satellite, IEEE Trans. Geosci. Remote Sens., 44, 1075–1092, https://doi.org/10.1109/Tgrs.2006.873771, 2006.

https://doi.org/10.5194/gmd-2020-102
Preprint. Discussion started: 24 June 2020
© Author(s) 2020. CC BY 4.0 License.

Winker, D. M. and Pelon, J.: The CALIPSO mission, in: IEEE International Geoscience and Remote Sensing Symposium. Proceedings, vol. 2, pp. 1329–1331, https://doi.org/10.1109/IGARSS.2003.1294098, 2003.

Winker, D. M., Hunt, W. H., and McGill, M. J.: Initial performance assessment of CALIOP, Geophys. Res. Lett., 34, https://doi.org/10.1029/2007gl030135, 2007.

Winker, D. M., Vaughan, M. A., Omar, A., Hu, Y. X., Powell, K. A., Liu, Z. Y., Hunt, W. H., and Young, S. A.: Overview of the CALIPSO Mission and CALIOP Data Processing Algorithms, J. Atmos. Oceanic Technol., 26, 2310–2323, https://doi.org/10.1175/2009jtecha1281.1, 2009.

Wohltmann, I., Lehmann, R., and Rex, M.: The Lagrangian chemistry and transport model ATLAS: simulation and validation of stratospheric chemistry and ozone loss in the winter 1999/2000, Geosc. Model Dev., 3, 585–601, https://doi.org/10.5194/gmd-3-585-2010, 2010.

Zhu, Y. Q., Toon, O. B., Pitts, M. C., Lambert, A., Bardeen, C., and Kinnison, D. E.: Comparing simulated PSC optical properties with CALIPSO observations during the 2010 Antarctic winter, J. Geophys. Res., 122, 1175–1202, https://doi.org/10.1002/2016jd025191, 2017.